Electronic Supplementary Information

Recyclable and CO_2-retardant Zn-air Batteries Based on CO_2-decorated Highly Conductive Cellulose Electrolytes

Qinbo Liu,[†a] Xu Ou,[†a] Legeng Li,[a] Xiang Wang,[a] Jin Wen,[a] Yingjie Zhou*[a] and Feng Yan*[a,b]

[a]State Key Laboratory for Modification of Chemical Fibers and Polymer Materials, College of Materials Science and Engineering, Donghua University, Shanghai 201620, China

[b]Jiangsu Engineering Laboratory of Novel Functional Polymeric Materials, Department of Polymer Science and Engineering, College of Chemistry, Chemical, Engineering and Materials Science, Soochow University, Suzhou 215123, China

E-mail: zhouyj@dhu.edu.cn, fyan@suda.edu.cn

[†] These authors contributed equally.

Supplementary Text

Materials

Microcrystalline cellulose (CC, Rhawn, particle size: ~25 μm) was vacuum dried at 60 ℃ for 24 h before the usage. 1,8-diazabicyclo[5.4.0]undec-7-ene (DBU, Adamas, 98%), dimethyl sulfoxide (DMSO, Greagent, ≥99%), epichlorohydrin (ECH, Rhawn, 99.7%), zinc acetate ($Zn(CH_3COO)_2$, Greagent, >99%), sodium hydroxide (NaOH, Greagent, >96%), glycerol (Rhawn, 99%), sulphuric acid (H_2SO_4, Greagent, 95~98%), ethanol (Greagent, ≥99.7%), urea (Greagent, ≥99%), and potassium hydroxide (KOH, Greagent, ≥85%), 3,5-dinitrosalicylic acid (Rhawn, 98%) were used as received. CO_2 (Purity: >99.999%) was supplied from Shenzhong Gas Co., Ltd. (Shanghai, China).

Characterization

The surface morphology of products and mapping were investigated by Field Emission Scanning Electron Microscope (SEM, SU8010, Hitachi, Japan) equipped with elemental

mapping capability. Fourier transform-infrared spectra (FTIR, Nicolet iS50, USA) were collected using a universal attenuated total reflectance sampling accessory in the frequency range of 525-4000 cm^{-1}. Nuclear magnetic resonance spectra were recorded on a digital nuclear magnetic resonance spectrometer (AVANCE IIITM HD 600MHz, Bruker, Switzerland) in DMSO-d_6, LiCl/DMSO-d_6, or D_2O using TMS as an internal standard. X-ray diffraction (XRD) patterns were obtained over 2θ ranging from 10 to 90 ° at a scanning rate of 5 °·min^{-1} on a Powder X-ray diffractometer (Bruker D2 Phaser/D2 phaser, Germany). X-ray photoelectron spectroscopy (XPS) was carried out on Escalab (250Xi, USA) apparatus with C1s signal (284.8 ev) as the standard. The UV-vis absorption spectra were collected using a SHIMADZU UV-2600i (Japan) spectrophotometer (200-800 nm).

Water uptake and water retention capacities

The water uptake and water retention capacities of hydrogels were investigated at 35 ℃. The water uptake (W_u) and retention values (W_r) of hydrogel were calculated by the following equations (1-2):

$$W_u = \frac{W_1 - W_0}{W_0} \qquad (1)$$

$$W_r = \frac{W_2 - (W_3 - W_t)}{W_2} \qquad (2)$$

Where W_o is the weight of the dried hydrogel, W_1 is the weight of saturated hydrogel soaked in deionized water for 24 h. W_2 is the initial water weight of hydrogel and W_3 is the initial weight of the hydrogel. The extra water on the surface of all hydrogels was rubbed off with filter papers. All hydrogels were packed with films with vent holes to simulate the fabricated Zn-air batteries.

Electrochemical properties evaluation

Ionic conductivities

The ionic conductivities of the hydrogel electrolytes were investigated through impedance spectroscopy (EIS) with a frequency ranging from 100 kHz to 0.1 Hz on a CHI660E electrochemical workstation (Chenhua Instrument, China). The electrolyte was sandwiched between two symmetrical blocking stainless steel electrodes. The ionic conductivity (δ) was determined from the following equation (3):

$$\delta = \frac{L}{A \times R} \qquad (3)$$

where L is the distance between the two electrodes, A is the effective overlapping area of two electrodes, and R is the bulk resistance obtained from Nyquist plots.

Fabrication of Zn-Air Batteries (ZABs)

Air cathodes were prepared by coating catalyst ink onto carbon cloth, then dried at 60 ℃ for 24 h. The typical mass loading of catalysts was 0.75 mg·cm^{-2}, consisting of 6.91 mg of Co_3O_4, 13.82 mg of carbon black, 100 μL Nafion solution, 600 μL ethanol, and 600 μL isopropanol. ZABs were fabricated through a layer-by-layer procedure (Zn anode - hydrogel electrolyte - air cathode).

Anode and cathode for the recycled CC-CO_2 electrolyte-based Zn-air batteries were obtained from the spent batteries through polishing and washing, respectively.

Electrochemical performances of Zn-air batteries

To evaluate the performance of the Zn-air batteries, galvanostatic discharge, charge measurements, and the galvanostatic charge-discharge cycling test at a lower current density of 1 mA·cm^{-2} for 10 min and higher current density of 2 mA·cm^{-2} for 30 min were performed in a multichannel battery testing system (Landian CT2001A). The rate performance was determined at different current densities. All measurements were conducted under ambient atmosphere unless specifically mentioned.

Simulation

Gibbs free energy for the reaction of CC, CO_2, and DBU

To determine the reaction process, CO_2, DBU, and polymer chain units were selected from an equilibrium state in molecular dynamics (MD) simulations as the initial positions of the reaction in the geometry optimization. The contents of the component are listed in **Table S1,** which is determined by the mass percentage in experiments. These models were optimized at the B3LYP/cc-pVDZ level to simulate the reactants and products.[S1–S3] The transition states of these reactions were searched by the Synchronous Transit-Guided Quasi-Newton (STQN) method,[S4] which was carried out after the confirmation of the vibrational frequency calculations. These calculations were performed by Gaussian 09, Revision D.01.

Molecular Dynamics Simulations

The universal force field was chosen for metal ions in the system, and the MD simulations were performed in the Discover module in Materials Studio software in the version of 6.0. Firstly, energy minimization was taken to relax the system. Secondly, the Verlet integrator with a time step of 1 fs and the Nosé-Hoover thermostat for the temperature control in the NVT ensemble was taken to reach the system's equilibrium state. Finally, NPT simulation was carried out under

constant temperature (277.15K) and pressure (6.0 MPa) for 7 ns in the production step. Snapshots at every 50 ps were collected for the analysis in the solvent-accessible surface area (SASA). The mean square displacement (MSD) of OH^- and radial distribution function (RDF) were calculated for the whole equilibrium process. The contents of the different component are listed in **Table S2**, which is determined by the mass percentage in experiments.

Table S1. Contents of each component in the calculation models.

CO_2	DBU	CC
1900	250	10

Table S2. Contents of each component in the calculated model for the electrolyte.*

	H_2O	Zn^{2+}	OH^-	CH_3COO^-	K^+
CC electrolyte	3000	10	320	20	320
CC-CO_2 electrolyte	3000	10	320	20	320

*Each hydrogel contains 24 Glucose unit. The molar ratio of crosslinking agent (ECH) to anhydroglucose unit (AGU) in CC hydrogel was 0.8 while the molecular chain in CC-CO_2 hydrogel has 30% ionization degree, and the -[O-CO_2]$^-$ produced by ionization was cross-linked with Zn^{2+}.

Table S3. The solubility of sodium alginate-$Zn(CH_3COO)_2$ hydrogel in 6 M KOH.

Solute	Solvent	Crosslinking	Dissolution
Sodium Alginate	H_2O	-	√
Sodium Alginate	H_2O	2 M $Zn(CH_3COO)_2$	×
Sodium Alginate	6 M KOH	-	√
Sodium Alginate-Zn^{2+} gel	6 M KOH	-	×

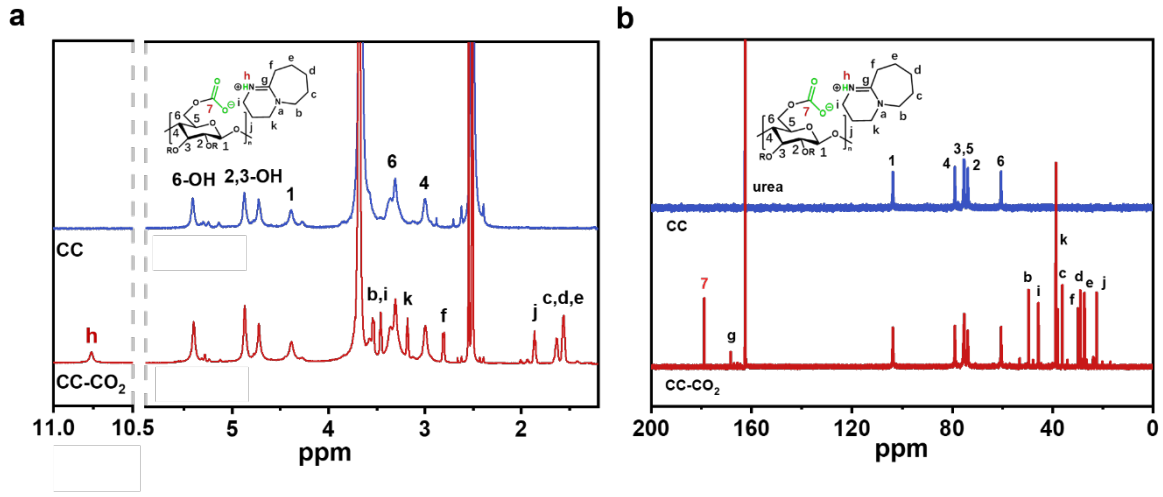

Fig. S1. The structure characterization with ^{1}H and ^{13}C NMR. (a) ^{1}H-NMR and (b) ^{13}C NMR spectra of CC and CC-CO_2.

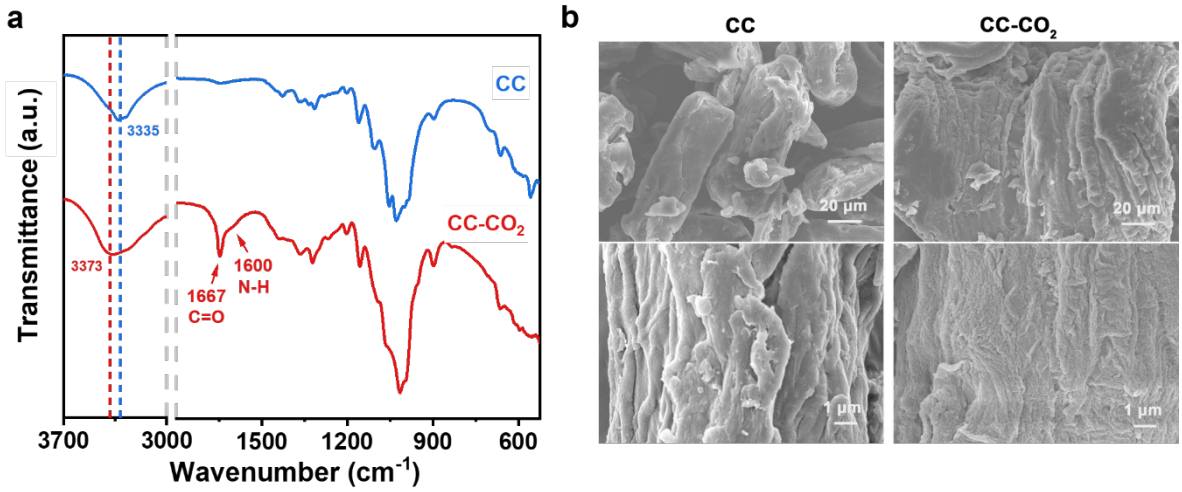

Fig. S2. The structure characterization of CC and CC-CO_2. (a) FTIR spectra and (b) SEM images of the neat CC and CC-CO_2.

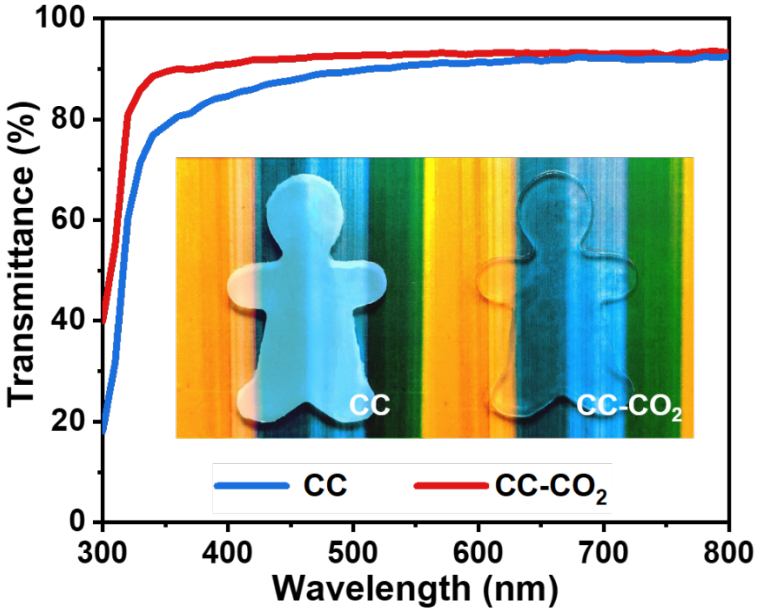

Fig. S3. UV-vis spectra of the CC and CC-CO_2 hydrogels, and insets are the digital photographs of CC and CC-CO_2 hydrogels.

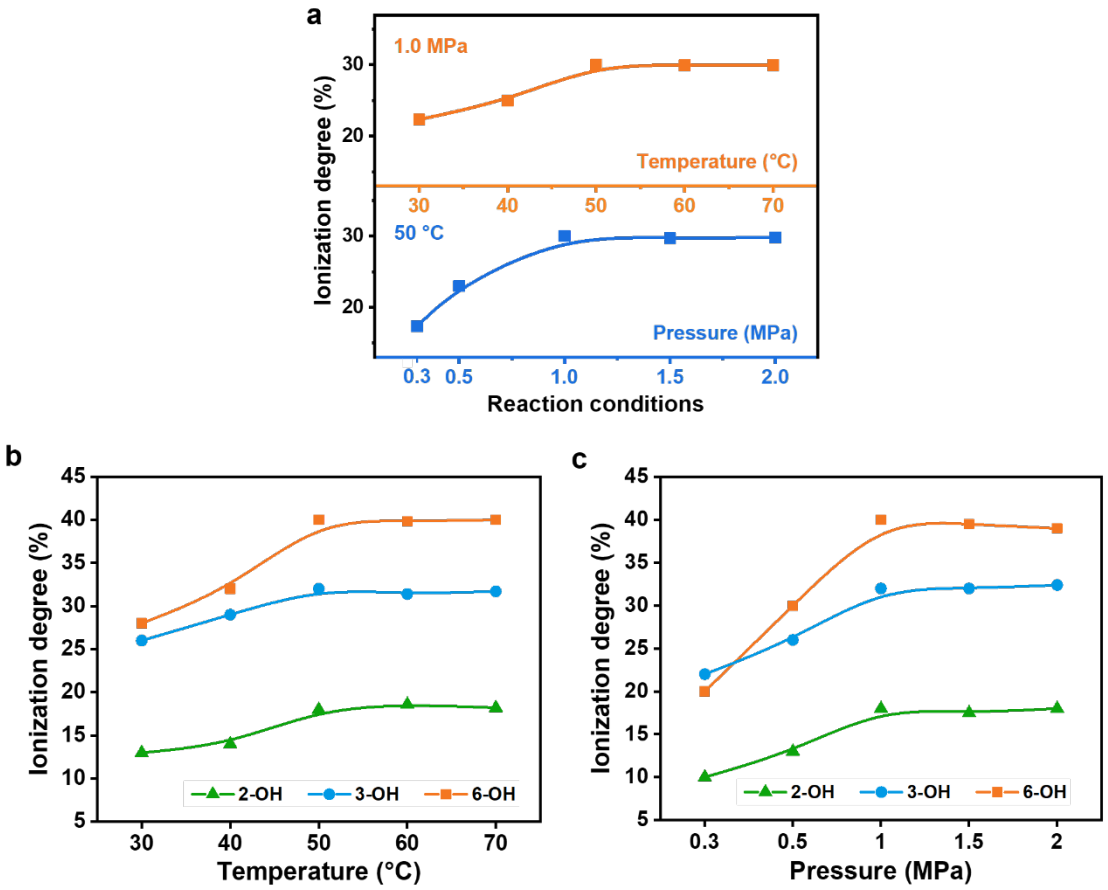

Fig. S4. Ionization degrees on different reaction conditions. (a) Influence of pressure and temperature on the total ionization degrees of the hydroxyl groups in CC. Influences of (b) temperature and (c) pressure on the ionization degrees for -OH on different positions of CC unit.

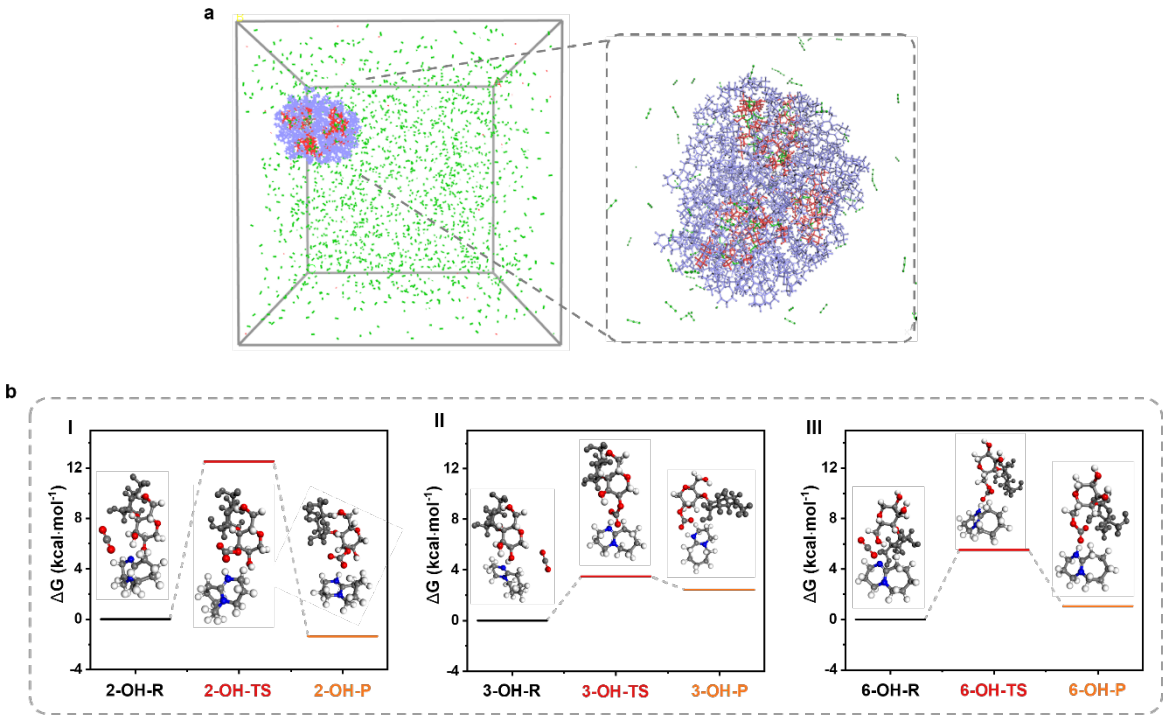

Fig. S5. Molecular dynamics (MD) simulation of the ionization reaction. (a) Snapshot and conformation analysis of the MD simulation of CC, DBU and CO_2, polymer chains are shown in colored spheres: CC, red; DBU, purple; CO_2, green. (b) Gibbs free energies of the ionized reactions between a molecular CO_2 and CC in CO_2-DBU-DMSO system (-OH groups at position 2, 3, and 6 were denoted as 2-OH, 3-OH, and 6-OH, R: reactant, TS: transition state; P: product) with the optimized molecular model.

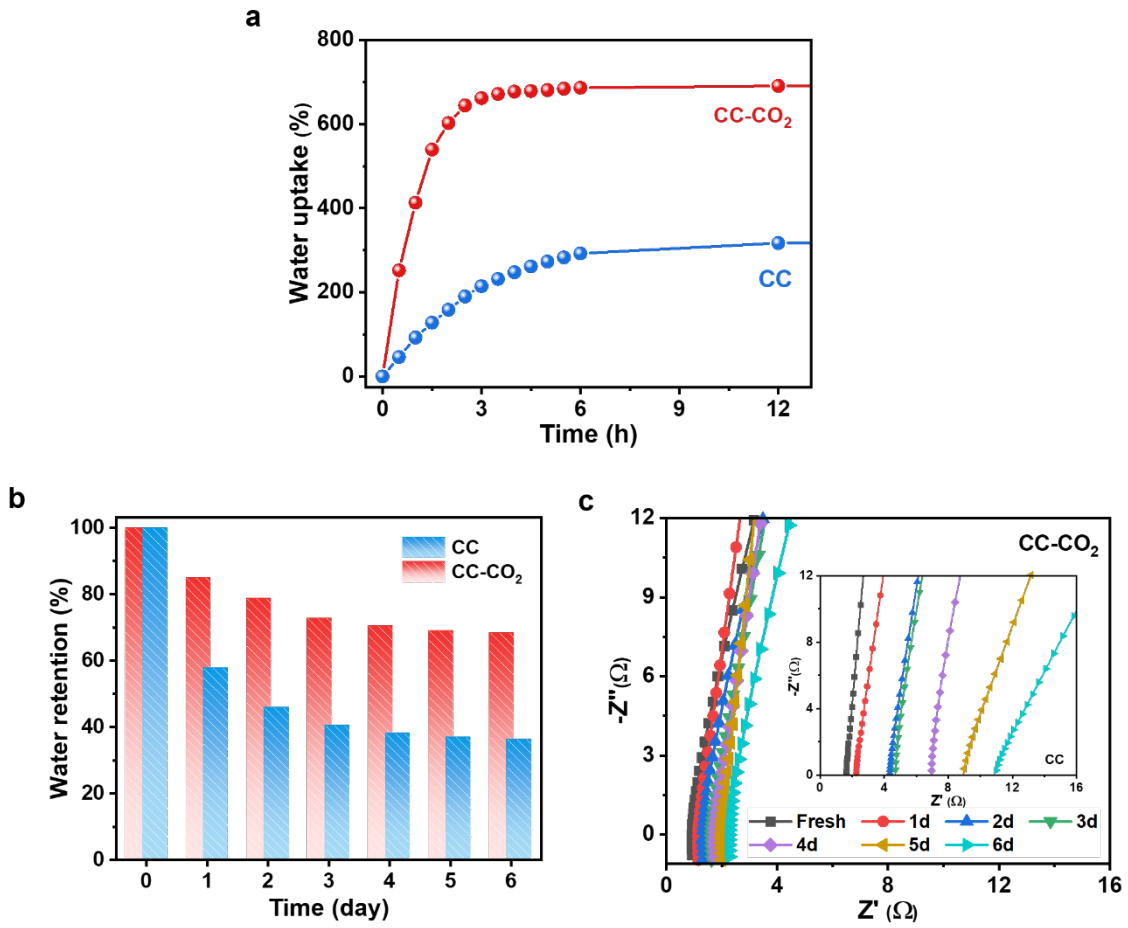

Fig. S6. Characterization of the hydrogels. (a) Magnified plots of water uptake of the CC and CC-CO_2 hydrogels. (b) Real-time water retention of CC and CC-CO_2 hydrogels, both hydrogels were encapsulated with a vented film and placed in a 35 °C oven for 6 days to simulate the working environment of Zn-air batteries. (c) Nyquist plots of CC and CC-CO_2 electrolytes, both electrolytes were sealed by plastic film with vented holes and kept in an oven (35 ºC, RH=35.3%).

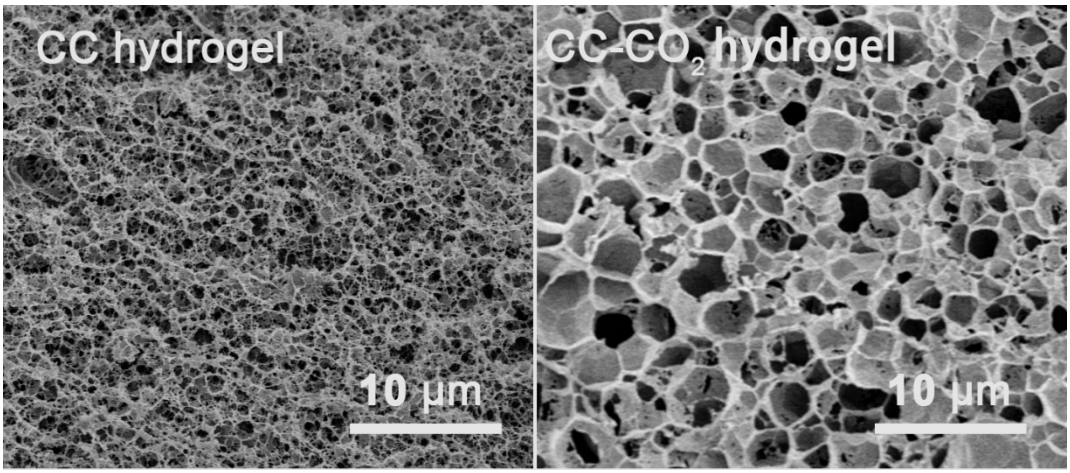

Fig. S7. SEM images of CC and CC-CO_2 hydrogels.

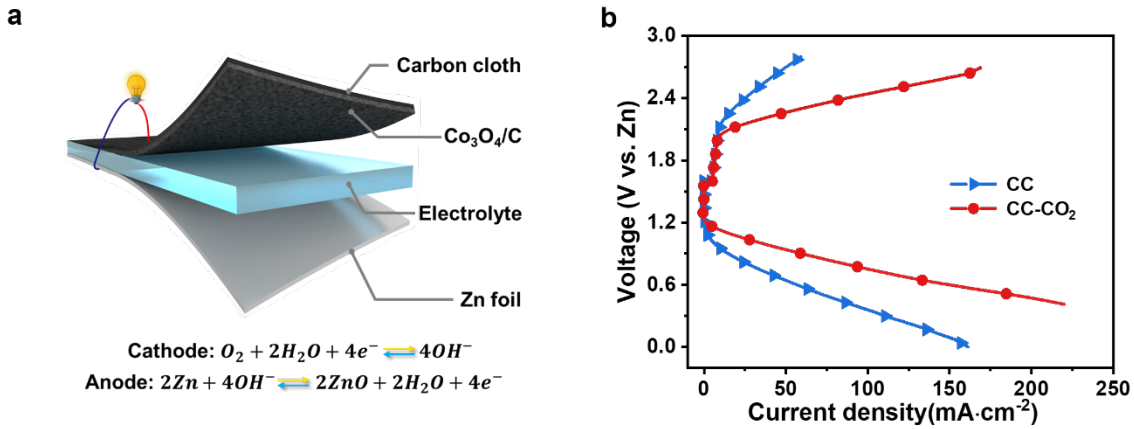

Fig. S8. The assembly and electrochemical performance of ZABs. (a) Schematic diagram of the flexible Zn-air battery comprising the Co_4O_3/C air cathode, hydrogel electrolyte and Zn anode. (b) Polarization curves of Zn-air batteries equipped with CC and CC-CO_2 hydrogel electrolytes.

Table S4. Summary of electrochemical performance of CC-CO_2 hydrogel electrolyte-based ZABs and other quasi/solid electrolytes in literatures.

References	Electrolyte	Power density ($mW \cdot cm^{-2}$)	Specific capacity ($mAh \cdot g^{-1}$)
This work	**CC-CO_2**	**95**	**779.7**
Adv. Energy Mater., 2018, 8, 180228[S5]	PANa	88	697
Adv. Energy Mater., 2021, 2102047[S6]	PVA-0.075TMG	84.1	812.9
J. Mater. Chem. A, 2019, 7, 11257–11264[S7]	PGG-GP	50.2	-
Energy Environ. Sci., 2016, 9, 663-670[S8]	2-QAFC	2362 $mW \cdot g^{-1}$	492
ACS Appl. Mater. Interfaces, 2019, 11, 28909−28917[S9]	TEAOH-PVA	-	657.9
J. Mater. Chem. A, 2019, 7, 17581–17593[S10]	P-AM	60	736
ACS Appl. Mater. Interfaces, 2018, 10, 29593−29598[S11]	CS-PDDA	48.9	-
ACS Appl. Mater. Interfaces, 2020, 12, 11778−11788[S12]	PAMPS-K25-MC	73.9	764.7

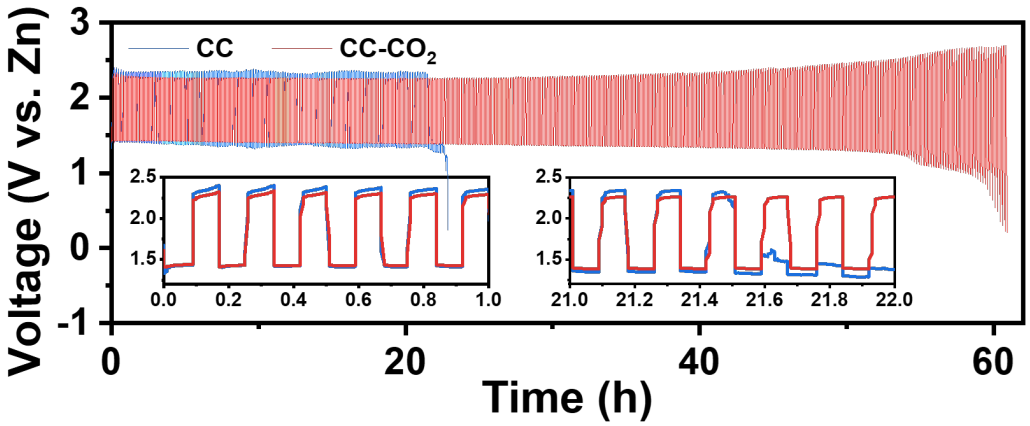

Fig. S9. Galvanostatic discharge-charge cycling curves at the specific cycling time (10 min per cycle) of Zn-air batteries in air at 1 mA·cm^{-2}.

Table S5. Summary of cycled charging/discharging testing conditions and results of CC-CO_2 hydrogel electrolyte-based ZABs and other quasi/solid electrolytes in literatures.

References	Electrolyte	Current density ($mA \cdot cm^{-2}$)	Time per cycle (min)	Cycle number	Cycle time (h)	Discharge capacity ($mAh \cdot g^{-1}$)
This work	**CC-CO_2**	**2**	**30**	**60**	**30**	**647.40**
This work	**CC-CO_2**	**1**	**10**	**336**	**56**	**222.22**
ACS Appl. Mater. Interfaces, 2019, 11, 28909−28917[S9]	TEAOH-PVA	5	20	105	35	208.3
J. Mater. Chem. A, 2019, 7, 17581–17593[S10]	P-AM	5	20	120	40	277.78
ACS Appl. Mater. Interfaces, 2018, 10, 29593−29598[S11]	CS-PDDA	3	10	16	2.7	125.32
Adv. Mater., 2016, **28**, 3000[S13]	PVA	2	10	36	6	-
J. Mater. Chem., A, 2019, 7, 11257–11264[S7]	PGG-GP	2	10	54	9	83.33
Nano Energy, 2013, **2**, 468[S14]	Cellulose	1	20	30	10	-
J. Am. Chem. Soc., 2016, **138**, 10226[S15]	PVA	0.5	20	36	12	416.67
Energy Environ. Sci., 2016, 9, 663-670[S8]	2-QAFC	0.25	60	35	35	191.18

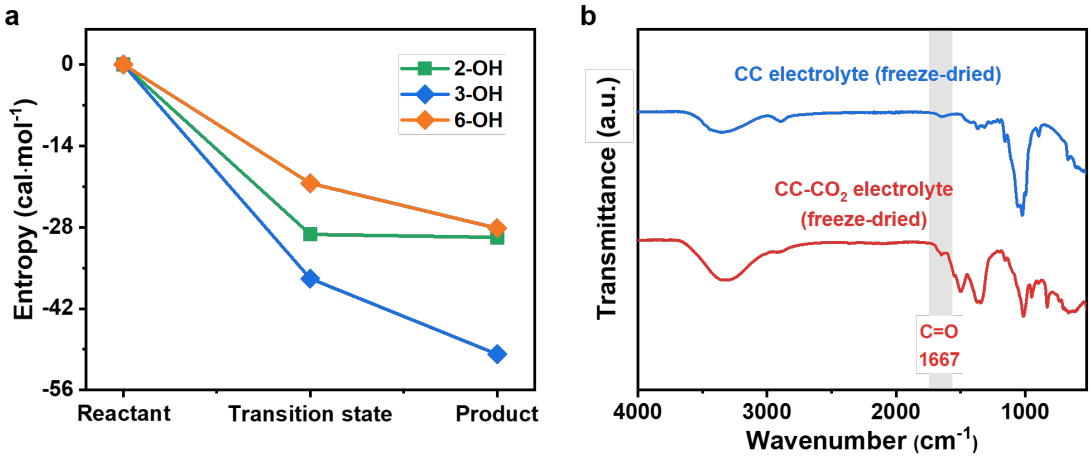

Fig. S10. Stability of CC-CO_2 and -[O-CO_2]$^-$ groups. (a) Entropy of the ionization reaction between CO_2 and CC in the CO_2-DBU-DMSO system. (-OH groups at position 2, 3, and 6 were noted as 2-OH, 3-OH, and 6-OH) (b) FTIR spectra of freeze-dried CC and CC-CO_2 electrolyte.

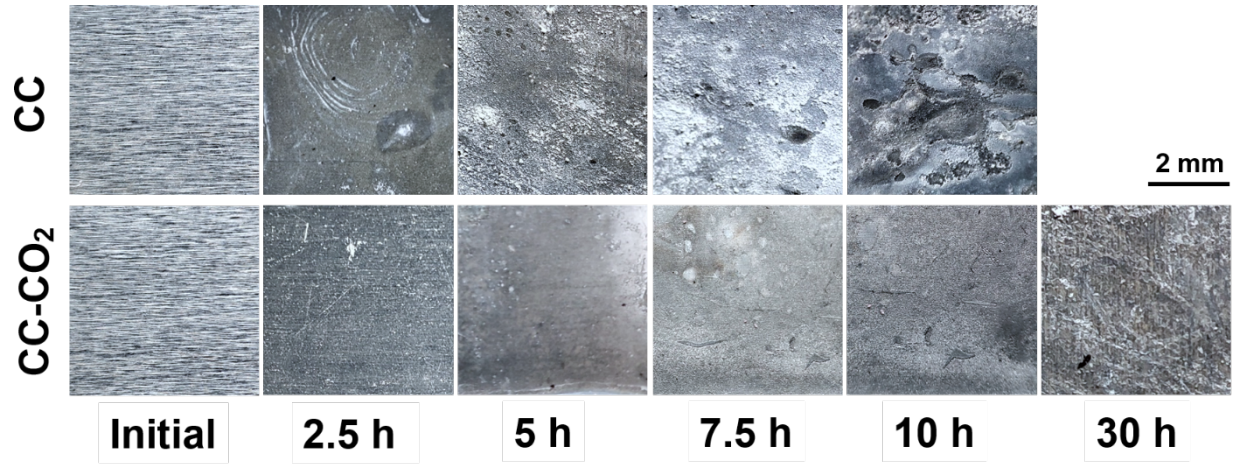

Fig. S11. Digital photographs of Zn anode of ZABs equipped with CC and CC-CO_2 electrolytes observed at various cycling time at 2 mA·cm^{-2} and 30 min per cycle.

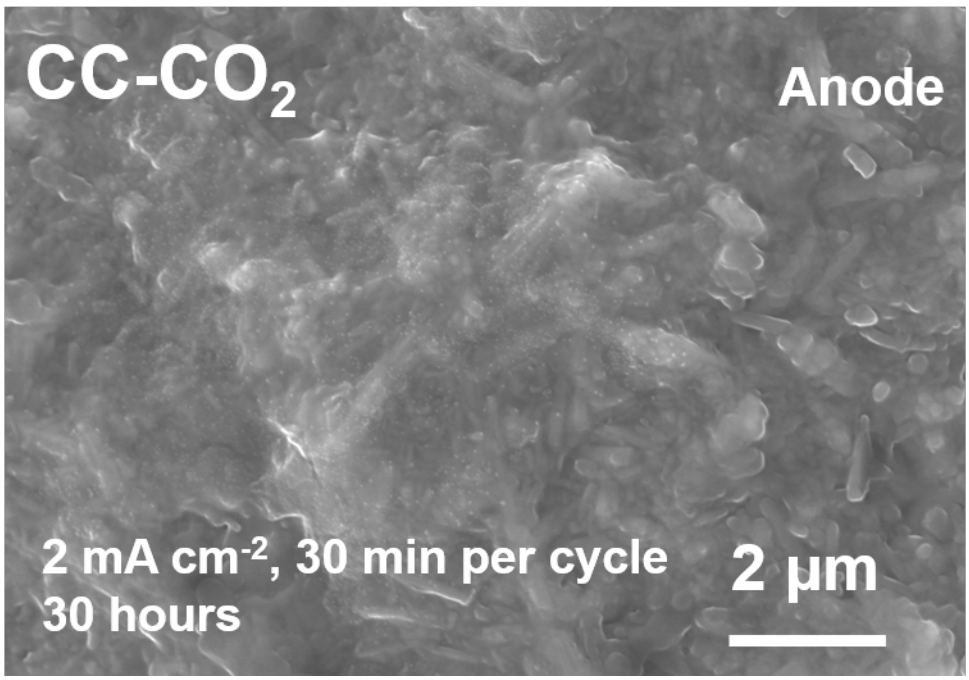

Fig. S12. SEM image of Zn anode recycled after 30 hours with CC-CO_2 electrolyte.

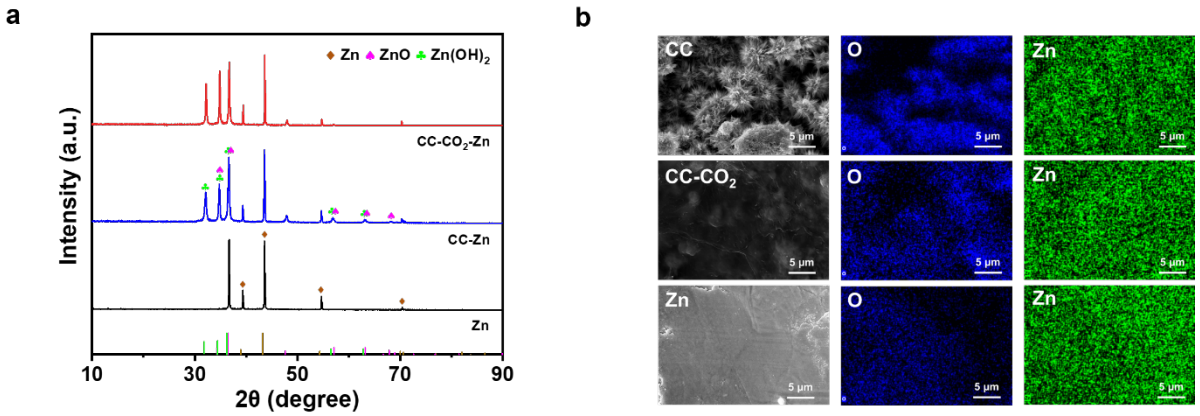

Fig. S13. Surface analysis of Zn anodes. (a) XRD patterns, (b) O and Zn mapping of the Zn anodes in the ZABs before and after being recycled for 10 hours with two types of electrolytes.

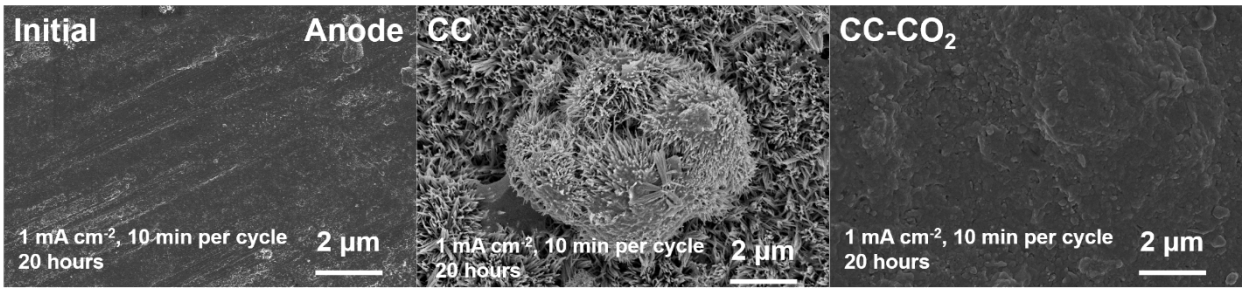

Fig. S14. SEM images of Zn anodes in the Zn-air batteries with CC and CC-CO_2 hydrogel electrolytes at 1 mA·cm^{-2} and 10 min per cycle before and after 20 hours.

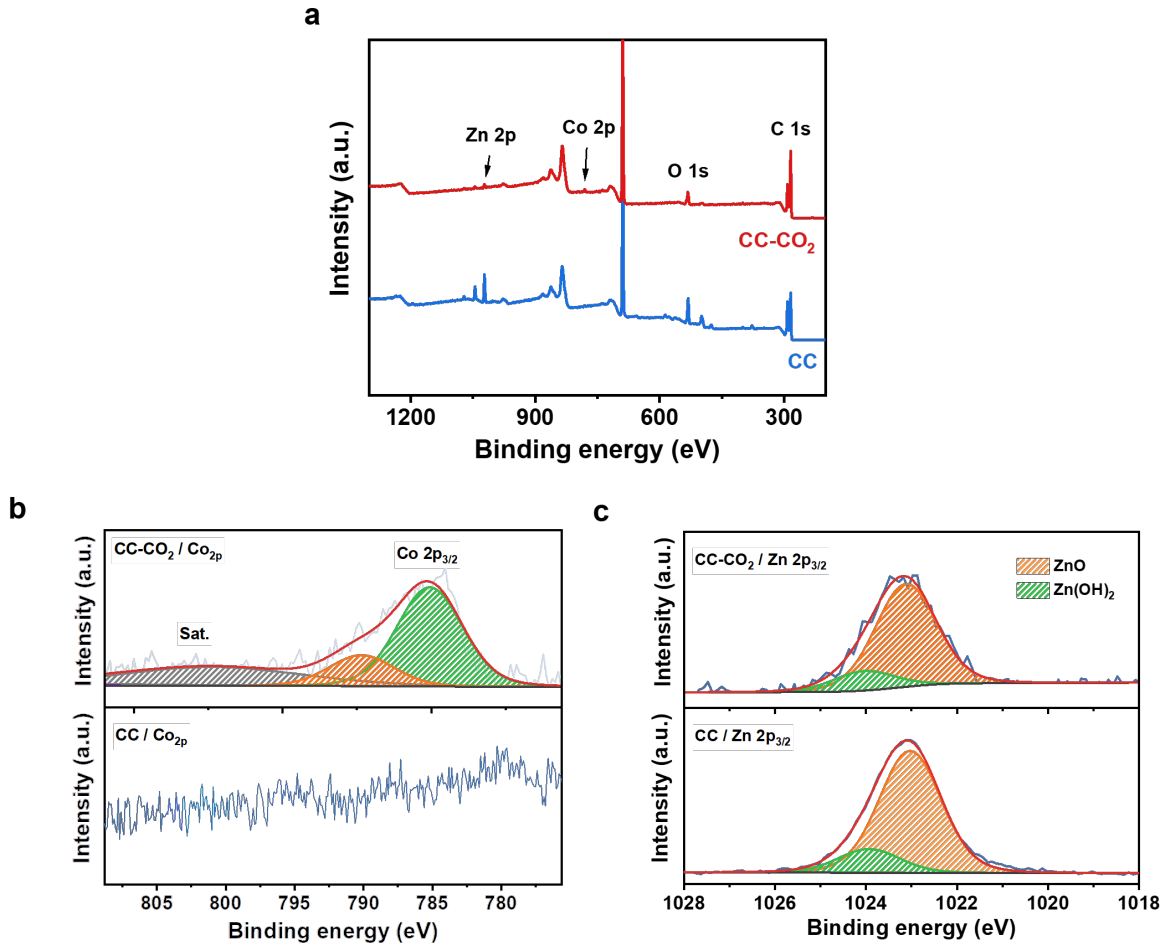

Fig. S15. Surface analysis of cathodes. (a) XPS survey spectra of the air cathode equipped with CC and CC-CO_2 electrolytes. High-resolution XPS spectra of (b) Co_{2p} and (c) Zn $2p_{3/2}$ of the air cathodes in the batteries equipped with CC and CC-CO_2 electrolytes.

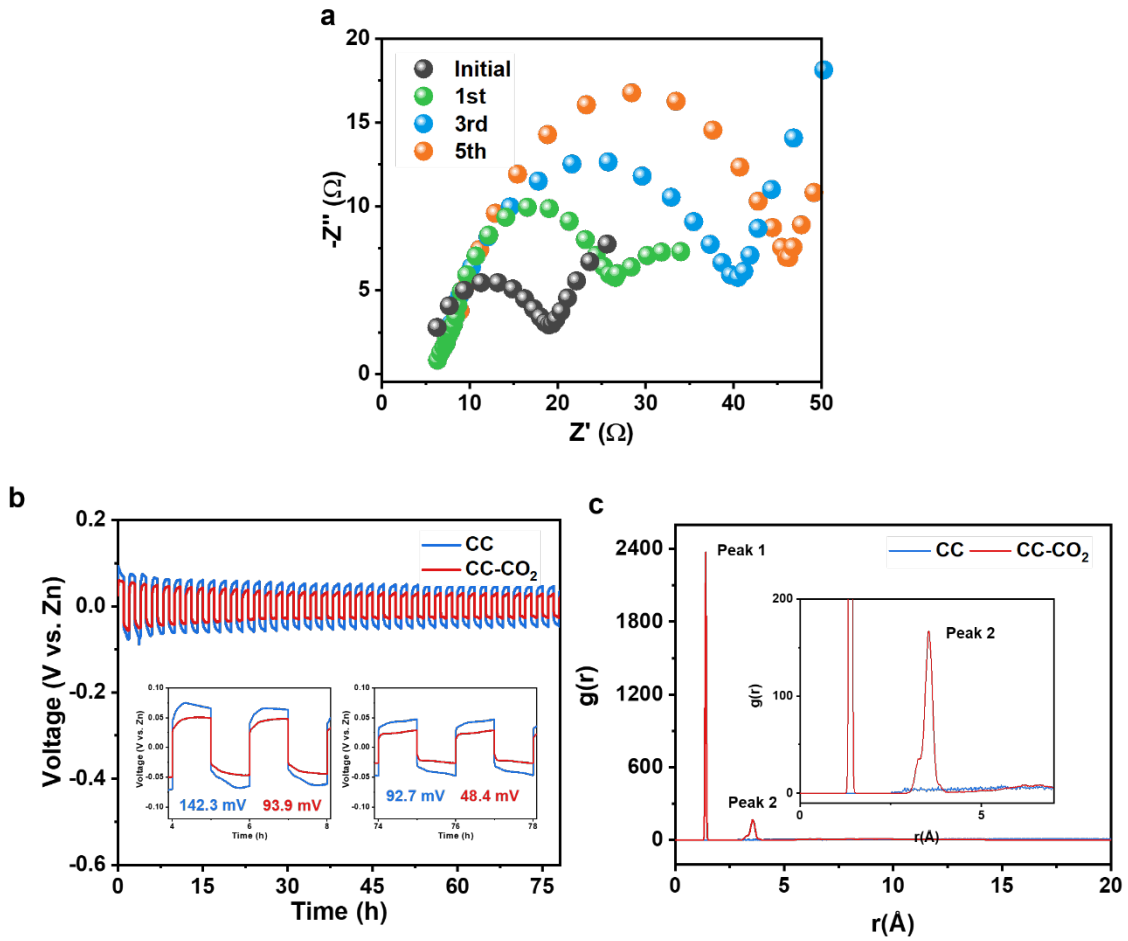

Fig. S16. Characterization of the intercalation and deintercalation of zinc ions in the electrode electrolyte boundary. (a) EIS of the Zn-air battery with CC electrolyte before and after 5 cycles. (b) Cycling stability of a Zn//Zn symmetrical cell with different hydrogel electrolyte in 2 M $Zn(CH_3COO)_2$ at 0.1 $mA \cdot cm^{-2}$ for 2 hours each cycle and the insets exhibit the magnified plots at different cycling time. (c) Radial distribution functions (RDF) of the interaction between the Zn^{2+} and -OH for CC or $-[O-CO_2]^-$ groups for CC-CO_2 electrolyte (Peak 1: Zn^{2+} in CC-CO_2 hydrogel electrolyte, peak 2: Zn^{2+} in electrolyte solution).

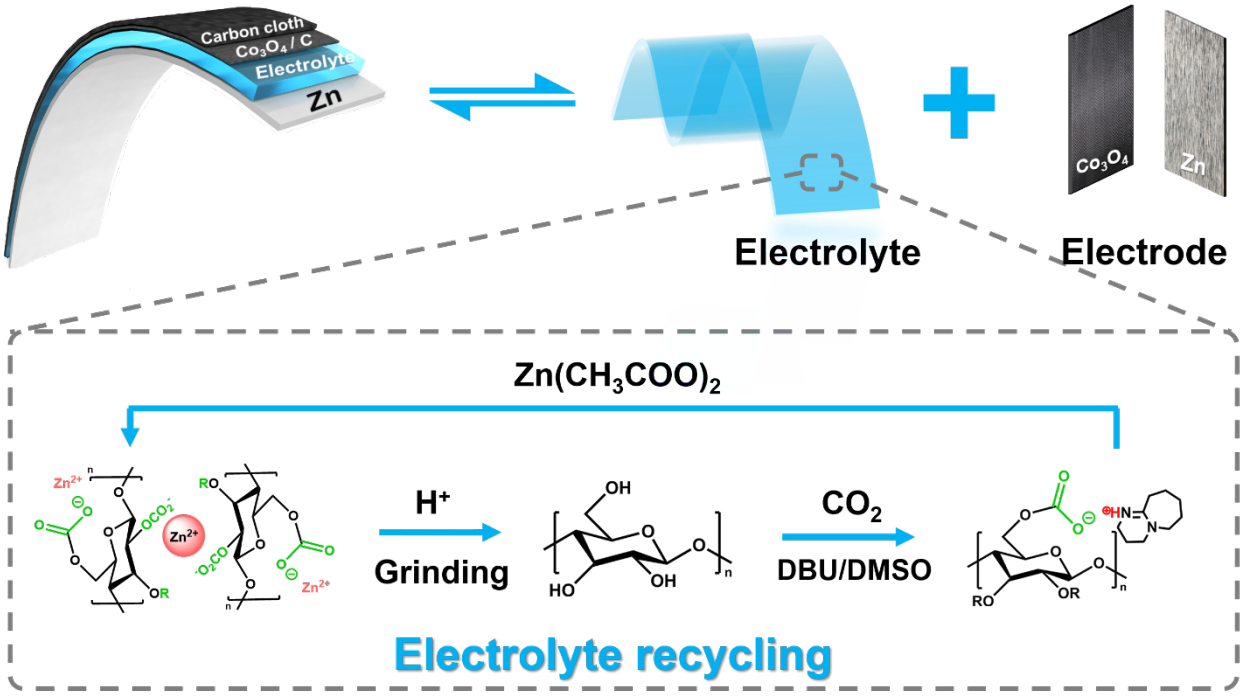

Fig. S17. Schematic diagram of the separation of Zn-air batteries with sandwiched structure and the recycling procedure of the CC-CO_2 hydrogel electrolyte.

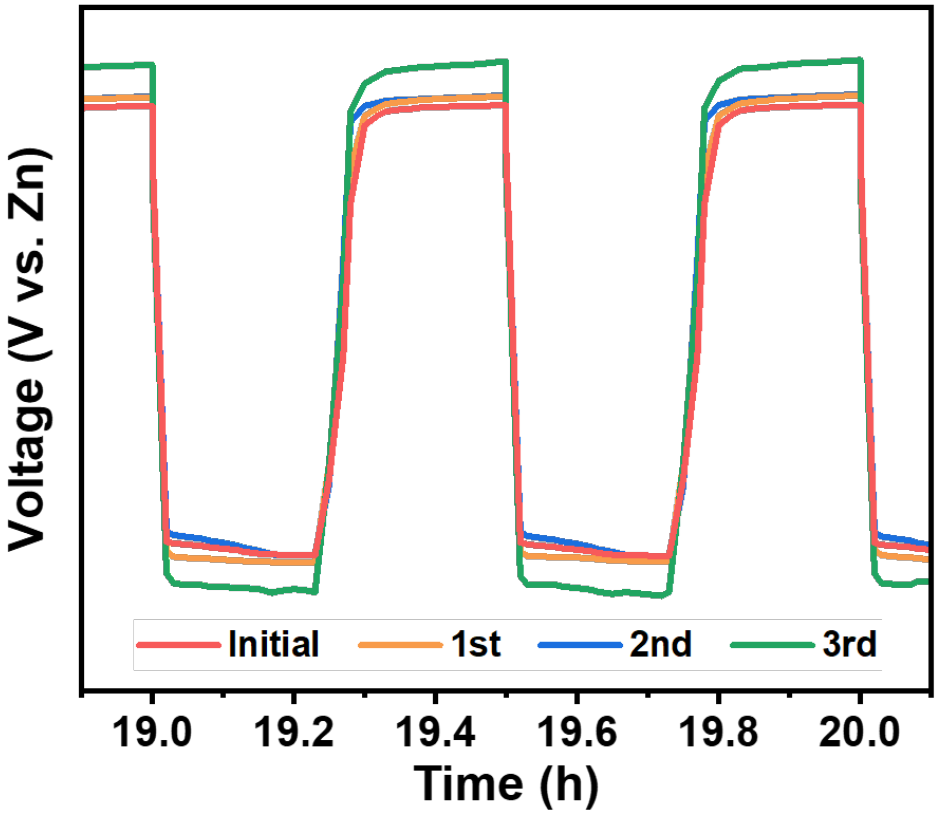

Fig. S18. Magnified plots of charge-discharge profiles of ZABs equipped with initial and recycled CC-CO_2 hydrogel electrolyte for three times at 2 mA·cm^{-2}.

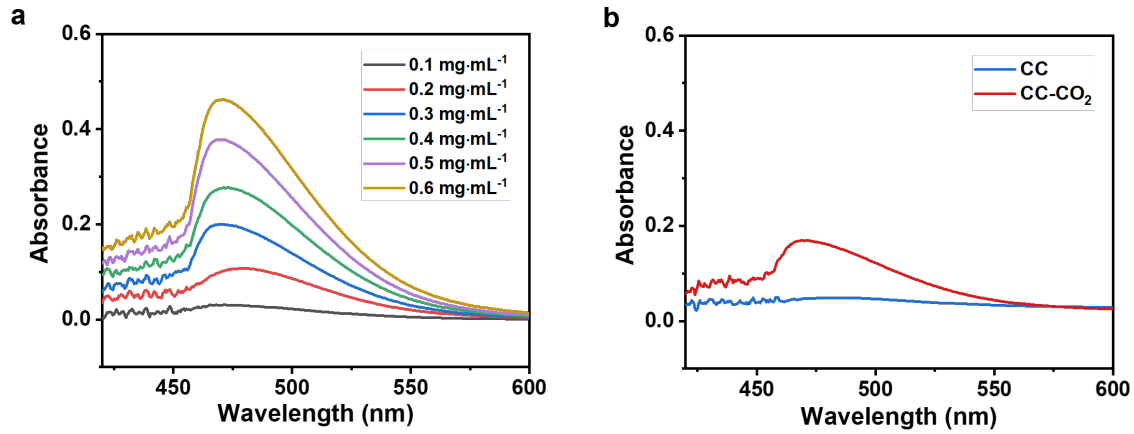

Fig. S19. Characterization of the degree of electrolyte degradation. UV-vis absorbance of (a) various glucose concentrations and (b) CC and CC-CO_2 degradation products after the color reaction.

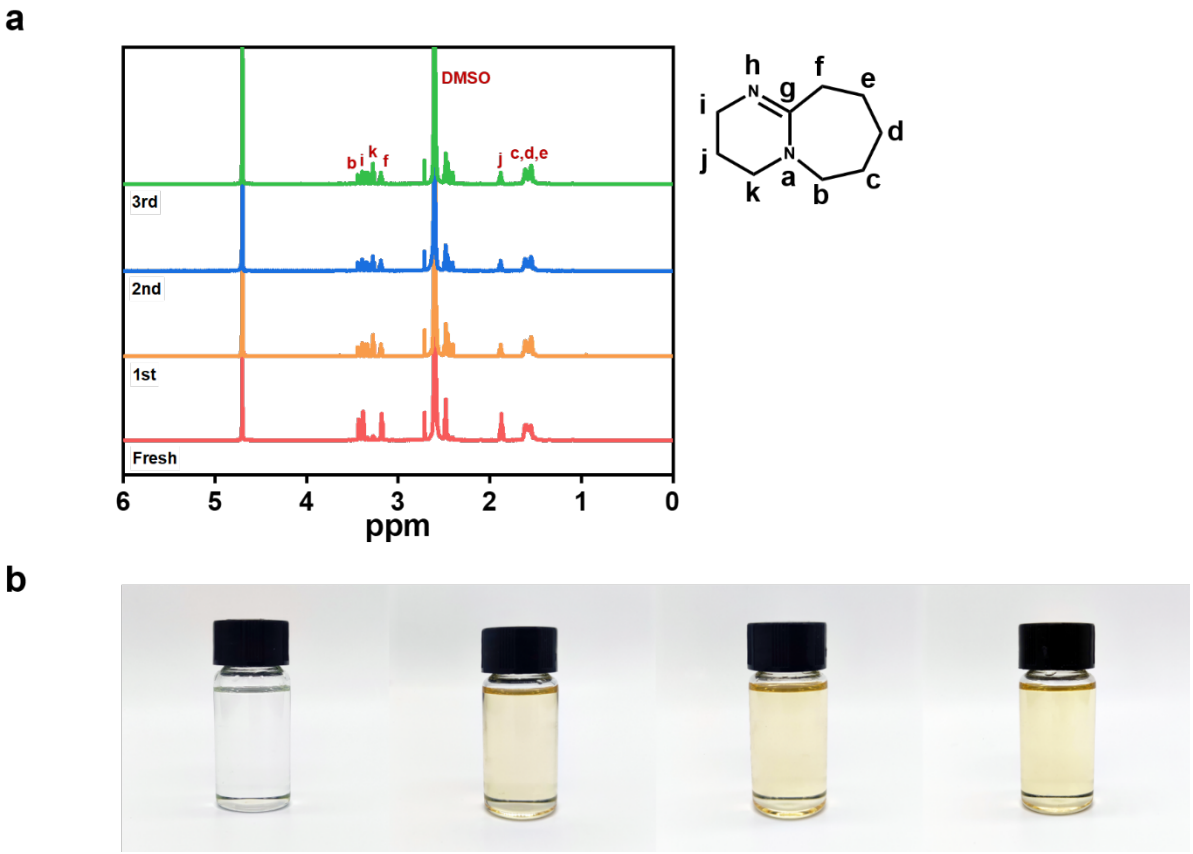

Fig. S20. Solvent recovery test. (a) ^{1}H-NMR spectra and (b) digital photographs of initial and recycled DBU-DMSO solvent at different recycles.

Movie S1. Transformation of Zn^{2+}, $Zn(OH)_2$ and $[Zn(OH)_4]^{2-}$

Movie S2. CO_2 bubbles evolved by acid treatment.

References:

S1 T. H. Dunning, *J. Chem. Phys.*, 1989, **90**, 1007–1023.
S2 C. Peng and H. Bernhard Schlegel, *Isr. J. Chem.*, 1993, **33**, 449–454.
S3 A. D. Becke, *J. Chem. Phys.*, 1993, **98**, 5648–5652.
S4 S. Grimme, J. Antony, S. Ehrlich and H. Krieg, *J. Chem. Phys.*, 2010, **132**, 154104.
S5 Y. Huang, Z. Li, Z. Pei, Z. Liu, H. Li, M. Zhu, J. Fan, Q. Dai, M. Zhang, L. Dai and C. Zhi, *Adv. Energy Mater.*, 2018, **8**, 1802288.
S6 Y. Zhou, J. Pan, X. Ou, Q. Liu, Y. Hu, W. Li, R. Wu, J. Wen and F. Yan, *Adv. Energy Mater.*, 2021, **11**, 2102047.
S7 M. Wang, N. Xu, J. Fu, Y. Liu and J. Qiao, *J. Mater. Chem. A*, 2019, **7**, 11257–11264.
S8 J. Fu, J. Zhang, X. Song, H. Zarrin, X. Tian, J. Qiao, L. Rasen, K. Li and Z. Chen, *Energy Environ. Sci.*, 2016, **9**, 663.
S9 M. Li, B. Liu, X. Fan, X. Liu, J. Liu, J. Ding, X. Han, Y. Deng, W. Hu and C. Zhong, *ACS Appl. Mater. Interfaces*, 2019, **11**, 28909–28917.
S10 Z. Cao, H. Hu, M. Wu, K. Tang and T. Jiang, *J. Mater. Chem. A*, 2019, **7**, 17581–17593.
S11 Y. Wei, M. Wang, N. Xu, L. Peng, J. Mao, Q. Gong and J. Qiao, *ACS Appl. Mater. Interfaces*, 2018, **10**, 29593–29598.
S12 N. Sun, F. Lu, Y. Yu, L. Su, X. Gao and L. Zheng, *ACS Appl. Mater. Interfaces*, 2020, **12**, 11778–11788.
S13 Q. Liu, Y. Wang, L. Dai and J. Yao, *Adv. Mater.*, 2016, **28**, 3000–3006.
S14 A. Kraytsberg and Y. Ein-Eli, *Nano Energy*, 2013, **2**, 468–480.
S15 F. Meng, H. Zhong, D. Bao, J. Yan and X. Zhang, *J. Am. Chem. Soc.*, 2016, **138**, 10226–10231.